advances
in radiation oncology

Scientific Article

Characterization of Markerless Tumor Tracking Using the On-Board Imager of a Commercial Linear Accelerator Equipped With Fast-kV Switching Dual-Energy Imaging

John C. Roeske, PhD,[a],* Hassan Mostafavi, PhD,[b]
Maksat Haytmyradov, PhD,[a] Adam Wang, PhD,[b] Daniel Morf, BS,[b]
Luca Cortesi, MSc,[b] Murat Surucu, PhD,[a] Rakesh Patel, PhD,[a]
Roberto Cassetta, PhD,[a] Liangjia Zhu, PhD,[b]
Mathias Lehmann, PhD,[b] and Matthew M. Harkenrider, MD[a]

[a]Department of Radiation Oncology, Loyola University Chicago, Maywood, Illinois; and [b]Varian Medical Systems, Palo Alto, California

Abstract

Purpose: To describe and characterize fast-kV switching, dual-energy (DE) imaging implemented within the on-board imager of a commercial linear accelerator for markerless tumor tracking (MTT).

Methods and Materials: Fast-kV switching, DE imaging provides for rapid switching between programmed tube voltages (ie, 60 and 120 kVp) from one image frame to the next. To characterize this system, the weighting factor used for logarithmic subtraction and signal difference-to-noise ratio were analyzed as a function of time and frame rate. MTT was evaluated using a thorax motion phantom and fast kV, DE imaging was compared versus single energy (SE) imaging over 360 degrees of rotation. A template-based matching algorithm was used to track target motion on both DE and SE sequences. Receiver operating characteristics were used to compare tracking results for both modalities.

Results: The weighting factor was inversely related to frame rate and stable over time. After applying the frame rate−dependent weighting factor, the signal difference-to-noise ratio was consistent across all frame rates considered for simulated tumors ranging from 5 to 25 mm in diameter. An analysis of receiver operating characteristics curves showed improved tracking with DE versus SE imaging. The area under the curve for the 10-mm target ranged from 0.821 to 0.858 for SE imaging versus 0.968 to 0.974 for DE imaging. Moreover, the residual tracking errors for the same target size ranged from 2.02 to 2.18 mm versus 0.79 to 1.07 mm for SE and DE imaging, respectively.

    * Corresponding author: John C. Roeske, PhD; E-mail: jroeske@lumc.edu.

Conclusions: Fast-kV switching, DE imaging was implemented on the on-board imager of a commercial linear accelerator. DE imaging resulted in improved MTT accuracy over SE imaging. Such an approach may have application for MTT of patients with lung cancer receiving stereotactic body radiation therapy, particularly for small tumors where MTT with SE imaging may fail.

Introduction

Markerless tumor tracking (MTT) is a technique that is being considering for the management of lung tumor motion. Unlike fiducial-based tracking,[1-6] MTT uses images to directly track the tumor. X-ray–based MTT may be performed using planar MV[7-9] or kV[10-15] images. In cases where the tumor is clearly visible, MTT has been shown to track tumors with a high degree of accuracy. However, in images where the bone overlaps the tumor at a particular imaging angle, MTT algorithms may have difficulty in differentiating tumor from bony anatomy.[10]

A potential solution to this problem is dual-energy (DE) imaging.[16-19] This technique involves obtaining fluoroscopic images at both high (ie, 120 kVp) and low (ie, 60 kVp) energies and then performing a weighted logarithmic subtraction to create a third image that removes bone and highlights soft tissue. Previous studies have shown improved tracking accuracy when combining DE imaging with MTT. Patel et al demonstrated that DE imaging improves both the accuracy and success rate of MTT versus single energy (SE) imaging.[18] In a separate study, Dhont et al showed improved contrast-to-noise ratio when using DE versus SE imaging.[20]

Although the previous studies demonstrated the potential of DE imaging, they were limited by the image acquisition protocol. In both cases, images were obtained sequentially, resulting in a significant time delay (on the order of seconds) between the 2 different energies. As such, these images were retrospectively analyzed to produce DE sequences. Clinically, this approach is not feasible, as it cannot be performed in real time and may introduce motion artifacts due to temporal registration errors. Recently, Haytmyradov et al examined the feasibility of performing MTT with DE imaging using fast-kV switching on a bench-top system.[21] In their study, they demonstrated this approach provided improved tracking, particularly for small targets versus SE imaging.

The goal of this study is to describe fast-kV switching, DE imaging as it has been implemented within the on-board imager (OBI) of a commercial linear accelerator. In the first published study of this kind, we characterize fast-kV switching using the OBI to perform MTT with DE subtraction.

Methods and Materials

Fast-kV switching, DE imaging

Images were obtained using the fast-kV switching capabilities of the OBI of a TrueBeam linear accelerator (Varian Medical Systems, Palo Alto, CA). The OBI system consists of an x-ray tube (GS 1542, Varex Imaging, Salt Lake City, UT) and generator (EPS 45-80, EMD Technologies, Saint-Eustache, Quebec) along with an amorphous-silicon (a-Si) flat panel detector (PaxScan 4030CB, Varex Imaging, Salt Lake City, UT). The software for fast-kV switching provides consecutive x-ray pulses that alternate between a programmed sequence and is accessed through Developer Mode (Varian Medical Systems, Palo Alto, CA) in version 2.7MR3 of the TrueBeam software. Through this scripting capability, the x-ray energy, milliamperes (mA), exposure time (milliseconds, ms), and frame rate are programmed for image acquisition. The allowed image acquisition rates are 3, 7, 11, and 15 frames per second (fps). The resultant DE frame rate is half of the programmed frame rate with each image pair resulting in one DE image.

Images quality was assessed using a fixed gantry angle while MTT was evaluated using a rotational sequence of 360 degrees over approximately 1 minute. During image acquisition, the source-to-axis distance was nominally set to 100 cm and the source-to-image distance was 150 cm. Images were acquired using a frame grabber system (Matrox Imaging, Quebec, Canada) for offline processing and encoded in 16-bit unsigned integers. All images have dimensions of 1024 × 768 pixels, with a pixel size of 0.388 mm, saved in the proprietary XIM format (Varian).

Image analysis

DE subtraction images were produced by performing weighted logarithmic subtraction using:

$$DE = ln\, I_h - w_s\, ln\, I_l \qquad (1)$$

where I_h and I_l are the intensity values in a given pixel for the high and low energy images respectively, whereas ln represents the natural logarithm and w_s is the weighting factor used to produce a soft tissue enhanced DE image.[16,21,22]

Image quality was assessed using a static phantom that was designed and built for optimizing DE imaging parameters.[21,22] Briefly, the phantom consists of material slabs with cylindrical inserts embedded within the tissue-equivalent slabs to mimic bone (ribs). Five simulated spherical tumors with diameters ranging from 5 to 25 mm are embedded in 2 of the lung-equivalent slabs. Figure 1 shows an image of the static phantom obtained at 120 kVp (left). The simulated bone materials are superimposed over the spherical targets, obscuring their visibility. Removal of the bone using DE imaging (right) clearly shows the simulated tumors.

To evaluate the effect of imaging frame rate and time, the static phantom was placed on the treatment table and set up at midplane. The OBI arms of the linac were extended and rotated to provide an anterior imaging angle with a source-to-surface distance (SSD) of 90 cm. Images were acquired at a fixed gantry angle based on imaging previously determined parameters (120 kVp, 60 mA, 20 ms, and 60 kVp,15 mA, 20 ms)[18,21,22] using an XML script that was executed in Developer Mode (Varian). To investigate the effect of acquisition time on weighting factors and image quality, images were acquired at the available frame rates (3, 7, 11, and 15 fps) for approximately 30 secs. For each DE image pair, the value of w_s (equation 1) was determined using an iterative method where regions of interest (ROI) were placed in bone and a nearby background region.[16,22] The weight was adjusted to minimize the difference between the bone and background ROI on the resultant DE image.

Image quality was assessed using the signal-difference-to-noise ratio (SDNR)[16,22]:

$$SDNR = \frac{S_{Tum} - S_{Bkd}}{\sqrt{\sigma_{Tum}^2 + \sigma_{Bkd}^2}} \quad (2)$$

where S_{Tum} and S_{Bkd} represent the mean signal in 10×10 pixel ROIs located at the center of the simulated tumor and in a background location, respectively. Similarly, σ_{Tum} and σ_{Bkd} represent the standard deviations within the same ROIs.

Markerless tumor tracking

MTT was performed using a template tracking algorithm[23] implemented in a noncommercial off-line research software (RapidTrack v3.0, Varian Medical Systems, Palo Alto, CA). This algorithm uses templates derived from a computed tomography (CT) scan of the target. For this study, the CIRS dynamic thorax motion phantom (CIRS Inc, Norfolk, VA) was used. This phantom mimics a human torso and includes 2 lung-equivalent cavities. One of the lung-equivalent cavities has a cylindrical insert that is driven by a motor and actuator. Within the cylindrical insert, simulated tumors ranging in size from 5 to 25 mm (steps of 5 mm) can be individually placed. Figure 2 shows a lateral SE image (left) of the phantom illustrating the overlap of the tumor with the spine and ribs. After the application of DE subtraction, the bony anatomy is removed (right), and the tumor contrast is improved. Respiratory motion is simulated by driving the cylindrical insert of the phantom using a programmable motion sequence ($\cos^4$). Three clinically relevant motion types were considered: stationary (simulating breath hold), slow motion (amplitude = 7.5 mm, period = 5 sec), and fast motion (amplitude = 7.5 mm, period = 2.5 sec).

For template-based tracking, a CT scan of the phantom was obtained on the department's CT simulator (Somatom Open AS, Siemens Healthineers, Germany) and reconstructed with the smallest slice thickness (0.6 mm). Subsequently, these images were transferred to the Eclipse software (version 15.5, Varian) where the targets were contoured using a lung window. The images and contours were then exported and input into RapidTrack Planning v1.12 (Varian) to produce the individual templates.

Phantom images were obtained while the gantry rotated 360 degrees in 1 minute. DE or SE sequences were then used with the templates to evaluate MTT. DE images were processed using equation 1, whereas SE images were obtained using only the 120 kVp images. The weighting factor was determined for each image pair
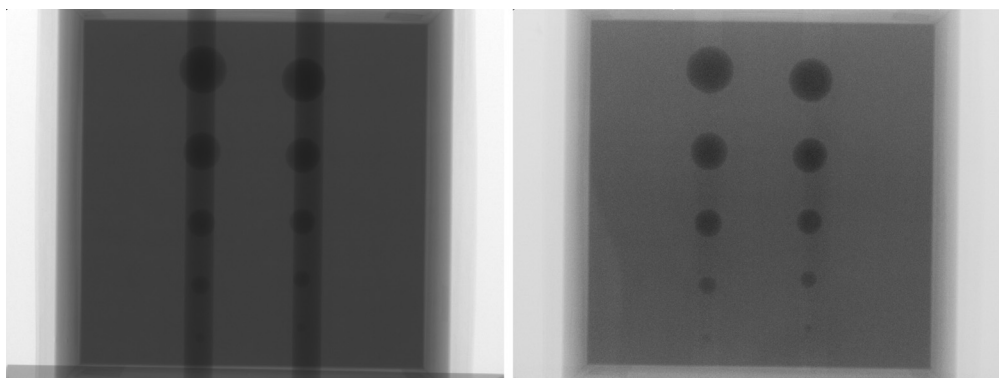
Figure 1 Single energy (120 kVp—left) and dual energy image (right) for the static phantom. Dual energy subtraction removes the simulated bones and highlights the individual targets ranging in size from 25 mm (superior) to 5 mm (inferior).
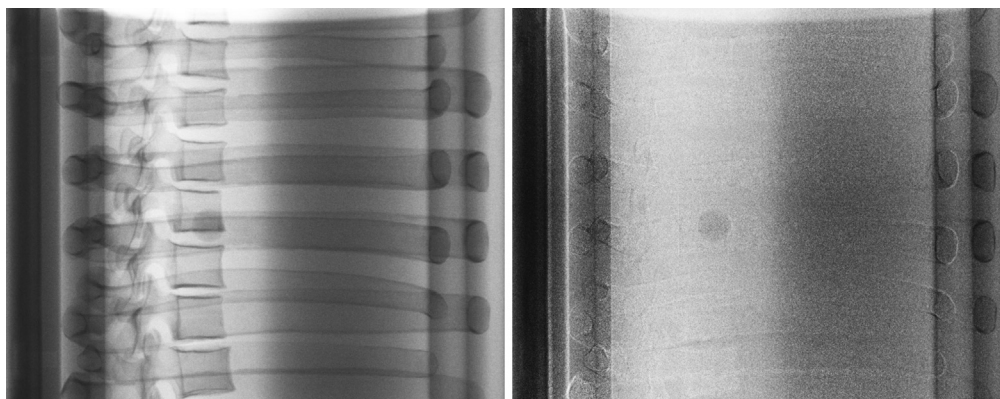
Figure 2 Single energy (left) and dual energy subtraction images (right) of the CIRS motion phantom obtained using a right lateral imaging angle.

based on the amount and type of bone in the projection as described previously.[21] For rotational acquisitions used for tracking, the offset between each image frame is ∼0.4 degrees at 15 fps, resulting in small misalignments between the high and low images. As such, rigid image registration was applied between frames using mutual information.[21,24] In general, the magnitude of the shifts between subsequent images was 1 to 2 pixels.[21] The time for DE subtraction was ∼19 ms per image pair.

Tracking was performed using an algorithm that scans the template across a search window centered on the expected position of the target in each projection. The window size is a 20-mm expansion of the template for each target size (ie, ± 10-mm search in each direction). At each template location, the normalized cross-correlation and match score are calculated.[23] Subsequently, a match score surface is produced. The location of the tracked tumor is determined by the position of the peak of the match score surface. The confidence level of the match is obtained by calculating the peak-to-side lobe ratio (PSR) from the match score surface.[23] The computational time for tracking is ∼47 to 73 ms/image.

Analysis of tracking results

To evaluate template matching, a novel analysis was performed based on the receiver operating characteristics (ROC). This process involves first determining the ground truth position as described by Haytmyradov et al.[21] Then, the distance between the tracked location and ground truth was determined for each tracking point. Values greater than a defined threshold were tagged as false positives, whereas distances with values less than or equal to the threshold were tagged as true positives.

Threshold values were determined by computing the autocorrelation of each template with itself and then calculating the width of the autocorrelation peak. The resultant thresholds were 1.3, 2.1, 2.5, 3.3, and 3.5 mm for the 5, 10, 15, 20, and 25 mm targets, respectively. In

this analysis, PSR was used as the discriminator to determine true positive fraction versus false positive fraction (FPF; 1, specificity). ROC analysis was performed using Excel (Microsoft, Redmond, WA). DE and SE-ROC curves were compared using the area under the curve (AUC). Local accuracy was calculated using the root mean square error of the true positives for an FPF ≤ 0.05.

Results

Figure 3 (left) shows the optimum weighting factor versus frame rate for the static phantom. The values represent the average weighting factors obtained over 30 sec of fluoroscopic imaging. As observed in the figure, there is an inverse relationship between weighting factor and frame rate, with the highest frame rate having the lowest weighting factor. The difference between the highest (3 fps) and lowest (15 fps) weighting factor is approximately 5%. For frame rates ≥7 fps, the variation in weighting factor is 1.3%.

The optimum weighting factor as a function of time for a 30 second imaging session is shown in Fig 3 (right) for an acquisition rate of 15 fps for the static phantom. The data for lower frame rates (3-11 fps) are consistent with these data, and therefore are not shown. As demonstrated in the figure, initially the weighting factor increases over the first 2 to 3 frames and then becomes nearly constant, with a slight increase of 0.5% over the 30 sec acquisition. Variations due to noise result in deviations of the weighting factor on the order of ± 0.5% with respect to the mean value, indicating good stability over time.

The effect of frame rate on SDNR is shown in Fig 4 for each of the 5 target sizes considered. For each frame rate, the weighting factor (Fig 3) is applied to produce the optimal DE subtraction image. As expected, the SDNR increases with target size, as the additional attenuation produced by the larger targets results in a more intense signal, relative to smaller targets. However, for a
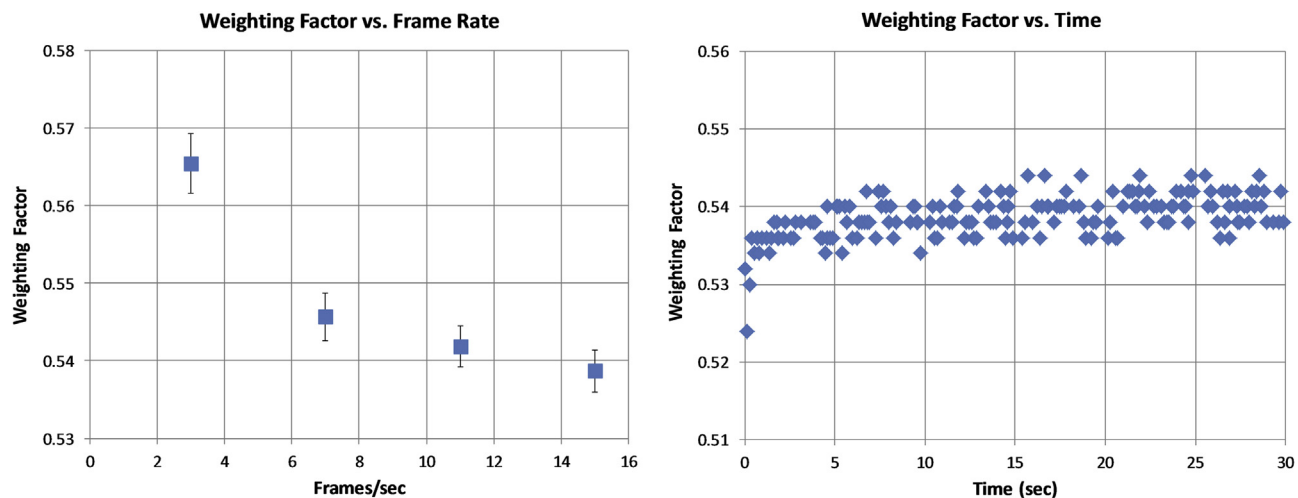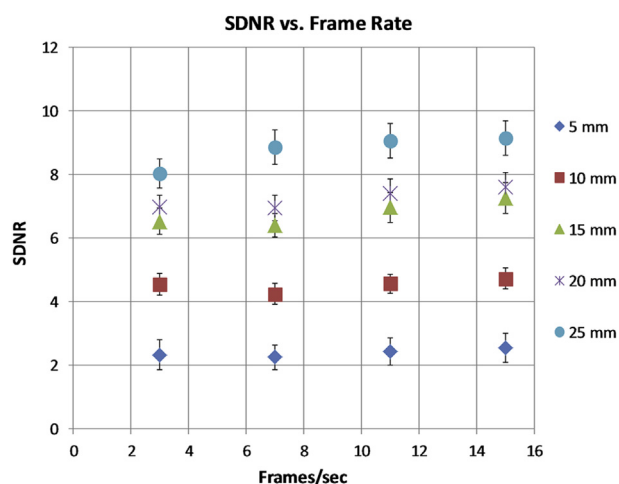
Figure 3   The average weighting factor obtained over 30 seconds plotted as a function of frame rate (left) and the weighting factor versus time acquired at 15 frames/s (right).

particular target size, the SDNR values do not change significantly with frame rate once the frame rate specific weighting factor is applied.

Figure 5 shows the ROC curves for each of the 5 targets for both DE and SE images for the fast motion case. The results are qualitatively similar for the other motion cases, and therefore are not presented. As observed in the figure, DE imaging results in a higher sensitivity versus SE imaging for nearly all specificity values. Of note, the largest differences are observed for the smallest targets (5 and 10 mm). Smaller differences are noted for the larger targets because these targets can be well visualized even in the presence of bone.

Table 1 provides a quantitative comparison using the AUC, PSR threshold, sensitivity (for a specificity of 95%), and local accuracy. In the idealized case, a test with perfect discrimination results in an AUC of 1, whereas a test with random discrimination has an AUC of 0.5. As shown in Table 1, DE imaging results in consistently higher AUC values versus SE imaging. This difference is larger for the smaller target sizes and diminishes for the larger targets, which is consistent with the visual analysis of the ROC curves. Using the ROC curves, the PSR threshold values were determined to result in a specificity of 95% (or 5% FPF). The resultant sensitivity values for this threshold are listed. Consistent with the prior results, DE imaging generally has increased sensitivity versus SE imaging. Additionally, a comparison of the local accuracy, which is the root mean square error of those true positive tracking events above the threshold PSR, shows that typically the DE values are smaller than the SE values, except for the largest target where they are comparable. As expected, the 5-mm target does not fare as well as the larger targets with reduced sensitivity and a higher local error. However, despite less than optimal tracking results in this target, DE-based MTT demonstrates superiority to SE tracking alone.

Discussion

In this study, we presented the characterization and phantom tracking results using fast-kV switching, DE imaging implemented within the OBI of a commercial linear accelerator. Fast-kV switching was implemented entirely using software (ie, there was no modification to the imaging or linac hardware). Hence, fast-kV switching can potentially be implemented on any TrueBeam linear accelerator equipped with the same x-ray generator used in this study.

Figure 4   Average signal-difference-to-noise ratio plotted as a function of frame rate for each of the spherical targets in the static phantom.
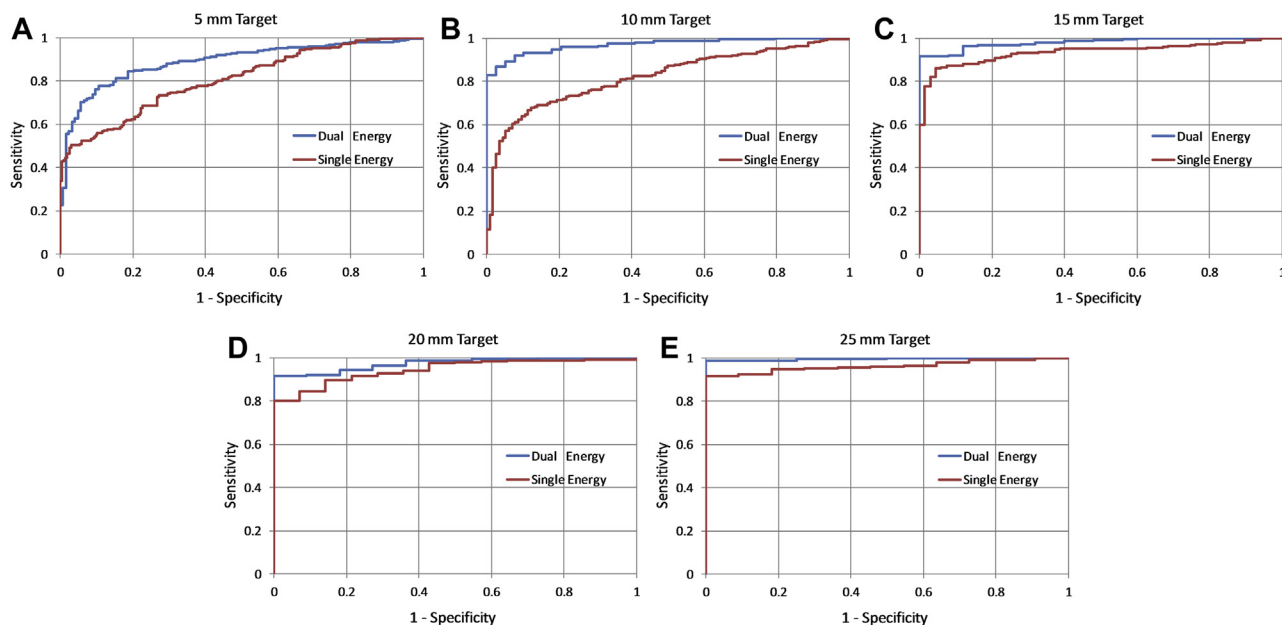
Figure 5   Receiver-operating characteristics for single and dual energy imaging for A) 5 mm; B) 10 mm; C) 15 mm; D) 20 mm; and E) 25 mm targets in the CIRS motion phantom.

In our analysis, it was noted that the weighting factor determined to suppress bone varied inversely with frame rate. We believe this effect is due to detector lag.[25,26] That is, as the frame rate is increased, there is a residual from the previous image that remains part of the next image due to the interplay between the exposure rate and the detector readout. However, the effect is small as the weighting factor changes only by a few percent, and the effect on SDNR is negligible as a function of frame rate. Moreover, our MTT analysis was performed using the highest frame rate and produced significant improvements in tracking over SE imaging. The use of lower frame rates

Table 1   Summary statistics for the receiver operating characteristic (ROC) of both single and dual energy images for the various types of motion considered

Size (mm)	AUC		PSR Threshold		Sensitivity		RMSE (mm)	
Stationary	SE	DE	SE	DE	SE	DE	SE	DE
5	0.753	0.829	2.76	3.17	0.47	0.46	3.59	2.49
10	0.858	0.974	3.37	3.32	0.64	0.88	2.18	0.79
15	0.908	0.976	3.77	3.53	0.71	0.91	0.99	0.49
20	0.903	0.935	3.81	3.68	0.73	0.87	0.23	0.33
25	0.937	0.956	3.99	3.91	0.77	0.92	0.33	0.34
Fast motion	SE	DE	SE	DE	SE	DE	SE	DE
5	0.829	0.888	2.73	3.15	0.57	0.63	2.91	2.20
10	0.845	0.968	3.53	3.72	0.50	0.83	2.05	0.89
15	0.918	0.969	3.92	3.84	0.66	0.86	0.52	0.32
20	0.919	0.964	3.82	3.69	0.81	0.93	0.38	0.33
25	0.956	0.993	3.41	3.88	0.89	0.99	0.43	0.33
Slow motion	SE	DE	SE	DE	SE	DE	SE	DE
5	0.806	0.889	2.73	3.02	0.50	0.66	3.74	2.24
10	0.821	0.969	3.49	3.52	0.54	0.87	2.02	1.07
15	0.935	0.943	3.44	3.48	0.86	0.92	0.56	0.40
20	0.943	0.973	3.73	3.74	0.80	0.92	0.34	0.29
25	0.961	0.994	3.45	3.96	0.92	0.99	0.37	0.33

Abbreviations: AUC = area under the curve; DE = dual energy; PSR = peak-to-side-lobe ratio; RMSE = root mean squared error; SE = single energy.

may reduce the effect of detector lag; however, motion artifacts may be introduced owing to the increased time between frames.

In the ROC analysis, PSR was used as a discriminator to predict sensitivity and local accuracy while maintaining a low false positive rate (<0.05). The clinical goal is to use PSR as a surrogate to assess tracking accuracy in real time. The PSR thresholds values measured in this study to achieve an FPF of 0.05 ranged from 2.73 to 3.99 for SE imaging and 3.02 to 3.99 for DE imaging. These values are consistent with a previous study by Block et al.[27] In their study based on images from 17 patients, it was determined that the false positive rate was 20.9% (PSR < 3) versus 4.0% (PSR ≥ 3; P <.01). It is important to note that Block et al results were based on clinical images that were obtained sequentially and processed offline. Temporal artifacts due to misalignment of the respiratory cycle may affect these results. However, unlike the phantom, which has idealized target shapes and anatomy, patient images have more variations. As such, future studies involving patient imaging and the estimation of tracking thresholds are required before such a technique can be implemented clinically.

A number of studies have investigated MTT using SE and DE imaging. Lewis et al used a template tracking approach for MTT in both phantom and patient SE images, with 95th percentile errors of 1.7 mm and 3.3 mm, respectively.[10] Of note, the authors pointed out that tracking errors up to 5 mm were observed in cases where the tumor overlapped with bone. As such, DE imaging may reduce the errors in these situations. Shieh et al removed bony anatomy by subtracting the background digitally reconstructed radiographs from SE kV images.[14,15] They subsequently evaluated a Bayesian approach in which an extended Kalman filter was used that combined prediction and measurement to estimate the tumor position.[15] Their approach resulted in 96.5% of images having errors <5 mm versus 84.1% using their standard of care. Such an approach can easily be incorporated into our DE imaging framework and may result in reduced errors, particularly for smaller tumors. Patel et al used fixed sequential DE imaging at a fixed gantry angle and observed and were able to track tumors on DE images with an accuracy of 1.4 ± 1.1 mm and 1.2 ± 0.6 mm in phantom and patient studies, respectively.[18] Haytmyradov et al recently performed template tracking using a fast-kV switching using a bench-top system.[21] They demonstrated improved tracking accuracy for smaller targets with success rates of 23% and 74% for SE imaging versus 64% and 90% with DE imaging for 5 and 10 mm targets, respectively.

The clinical implications of this research are significant. First, this technology may allow for fiducial markers to be avoided in those systems or clinical workflows in which they are currently being used. Fiducial markers can be placed either transbronchially (which is well tolerated but requires sedation and has limited application for peripheral tumors) or percutaneously (which carries additional potential morbidity but greater access to peripheral tumors).[28-32] Nevertheless, MTT obviates the need for an invasive procedure and any morbidity associated with implantation. For systems and workflows where fiducial markers are not necessary, MTT may allow for less adjacent normal tissue irradiation and lower integral dose to the patient by tracking the gross tumor volume directly. With less normal tissue irradiated, there is the potential for reduced clinically significant toxicity. At the same time, MTT allows for potential dose escalation of the gross tumor volume, which may be clinically effective in early stage lung cancer and other clinical scenarios.[33-35]

There are a number of limitations associated with this study. Among these is that in the fast-kV implementation, x-ray pulses are equally spaced. Future studies will investigate the optimization of frame rate to minimize the effects of detector lag and motion artifacts. Another consideration is that unlike tracking technologies that are not based on x-rays, fast-kV-based MTT adds additional dose to the patient. Based on a previous study, the additional dose to the skin (assuming 90 cm SSD) is approximately 1.022 mGy/s.[18,36] Although this additional dose may not be clinically significant, all efforts should be made to ensure that it is as low as reasonably possible and that the clinical benefits from MTT outweighs the additional dose. A final limitation is that all analysis was performed using simulated tumors that are spherical in shape. Departures from this idealized shape or changes in shape during the respiratory cycle may affect the accuracy of template tracking. Future phantom studies will involve the use of 3-dimensional printed tumors obtained from the planning scans of patients undergoing radiation therapy.

Conclusions

Fast-kV switching, DE imaging was implemented on the OBI of a commercial linear accelerator. DE imaging resulted in improved MTT accuracy over SE imaging. Such an approach may have application for MTT of patients with lung cancer receiving stereotactic body radiation therapy (SBRT), particularly for small tumors where MTT with SE imaging may fail.

References

1. Seiler PG, Blattmann H, Kirsch S, Muench RK, Schilling C. A novel tracking technique for the continuous precise measurement of tumour positions in conformal radiotherapy. *Phys Med Biol*. 2000; 45:N103-N110.
2. Sharp GC, Alexander B, Cui Y, Jiang SB, Dy JG. Robust fluoroscopic respiratory gating for lung cancer radiotherapy without implanted fiducial markers. *Phys Med Biol*. 2007;52:741-755.

3. Tang X, Sharp GC, Jiang SB. Fluoroscopic tracking of multiple implanted fiducial markers using multiple object tracking. *Phys Med Biol*. 2007;52:4081-4098.

4. Willoughby TR, Kupelian PA, Pouliot J, et al. Target localization and real-time tracking using the Calypso 4D localization system in patients with localized prostate cancer. *Int J Radiat Oncol*. 2006;65:528-534.

5. Kupelian P, Willoughby T, Mahadevan A, et al. Multi-institutional clinical experience with the Calypso System in localization and continuous, real-time monitoring of the prostate gland during external radiotherapy. *Int J Radiat Oncol*. 2007;67:1088-1098.

6. Booth JT, Caillet V, Hardcastle N, et al. The first patient treatment of electromagnetic-guided real time adaptive radiotherapy using MLC tracking for lung SABR. *Radiother Oncol*. 2016;121:19-25.

7. Serpa M, Baier K, Cremers F, Guckenberger M, Meyer J. Suitability of markerless EPID tracking for tumor position verification in gated radiotherapy. *Med Phys*. 2014;41:031702.

8. Bryant JH, Rottmann J, Lewis JH, Mishra P, Keall PJ, Berbeco RI. Registration of clinical volumes to beams-eye-view images for real-time tracking. *Med Phys*. 2014;41:121703.

9. Rottmann J, Keall P, Berbeco R. Markerless EPID image guided dynamic multi-leaf collimator tracking for lung tumors. *Phys Med Biol*. 2013;58:4195-4204.

10. Lewis JH, Li R, Watkins WT, et al. Markerless lung tumor tracking and trajectory reconstruction using rotational cone-beam projections: A feasibility study. *Phys Med Biol*. 2010;55:2505-2522.

11. Gendrin C, Furtado H, Weber C, et al. Monitoring tumor motion by real time 2D/3D registration during radiotherapy. *Radiother Oncol*. 2012;102:274-280.

12. Yang Y, Zhong Z, Guo X, et al. A novel markerless technique to evaluate daily lung tumor motion based on conventional cone-beam CT projection data. *Int J Radiat Oncol*. 2012;82:e749-e756.

13. van Sörnsen de Koste JR, Dahele M, Mostafavi H, et al. Markerless tracking of small lung tumors for stereotactic radiotherapy. *Med Phys*. 2015;42:1640-1652.

14. Shieh C, Keall P, Kuncic Z, Huang C, Feain I. Markerless tumor tracking using short kilovoltage imaging arcs for lung image-guided radiotherapy. *Phys Med Biol*. 2015;60:9437-9454.

15. Shieh C-C, Caillet V, Dunbar M, et al. A Bayesian approach for three-dimensional markerless tumor tracking using kV imaging during lung radiotherapy. *Phys Med Biol*. 2017;62:3065-3080.

16. Hoggarth MA, Luce J, Syeda F, et al. Dual energy imaging using a clinical on-board imaging system. *Phys Med Biol*. 2013;58:4331-4340.

17. Sherertz T, Hoggarth M, Luce J, et al. Prospective evaluation of dual-energy imaging in patients undergoing image guided radiation therapy for lung cancer: Initial clinical results. *Int J Radiat Oncol Biol Phys*. 2014;89:525-531.

18. Patel R, Panfil J, Campana M, et al. Markerless motion tracking of lung tumors using dual-energy fluoroscopy. *Med Phys*. 2015;42:254-262.

19. Dhont J, Poels K, Verellen D, et al. Feasibility of markerless tumor tracking by sequential dual-energy fluoroscopy on a clinical tumor tracking system. *IFMBE Proc*. 2015;51:591-594.

20. Dhont J, Verellen D, Poels K, et al. Feasibility of markerless tumor tracking by sequential dual-energy fluoroscopy on a clinical tumor tracking system. *Radiother Oncol*. 2015;117:487-490.

21. Haytmyradov M, Mostafavi H, Wang A, et al. Markerless tumor tracking using fast-kV dual energy fluoroscopy of a benchtop system. *Med Phys*. 2020;47:672-680.

22. Haytmyradov M, Patel R, Mostafavi H, et al. A novel phantom for characterization of dual energy imaging using an on-board imaging system. *Phys Med Biol*. 2019;64:03NT01.

23. Mostafavi H, Sloutsky A, Jeung A. Detection and localization of radiotherapy targets by template matching. In: *2012 Annual International Conference of the IEEE Engineering in Medicine and Biology Society. Vol 2012. IEEE*; 2012:6023-6027. https://doi.org/10.1109/EMBC.2012.6347367.

24. Cover TM, Thomas JA. *Elements of Information Theory*. Hoboken, NJ: Wiley-Interscience; 2006.

25. Stankovic U, Ploeger LS, Sonke JJ, Van Herk M. Clinical introduction of image lag correction for a cone beam CT system. *Med Phys*. 2016;43:1057-1064.

26. Sato H, Kondo K, Kato K, Nakazawa Y. Evaluation of image lag in a flat-panel, detector-equipped cardiovascular x-ray machine using a newly developed dynamic phantom. *J Appl Clin Med Phys*. 2015;16:366-375.

27. Block AM, Patel R, Surucu M, Harkenrider MM, Roeske JC. Evaluation of a template-based algorithm for markerless lung tumour localization on single- and dual-energy kilovoltage images. *Br J Radiol*. 2016;89:20160648.

28. Trumm CG, Haubler SM, Muacevic A, et al. CT fluoroscopy-guided percutaneous fiducial marker placement for cyberknife stereotactic radiosurgery: Technical results and complications in 222 consecutive procedures. *J Vasc Interv Radiol*. 2014;25:760-768.

29. Bhagat N, Fidelman N, Durack JC, et al. Complications associated with the percutaneous insertion of fiducial markers in the thorax. *Cardiovasc Intervent Radiol*. 2010;33:1186.

30. Majid A, Palkar A, Kheir F, et al. Convex probe EBUS-guided fiducial placement for malignant central lung lesions. *J Bronchol Interv Pulmonol*. 2018;25:283-289.

31. Belanger AR, Zagar T, Akulian JA. Convex endobronchial ultrasound-guided fiducial placement for malignant central lung lesions: A case series. *J Bronchol Interv Pulmonol*. 2016;23:46-50.

32. Lischalk JW, Woo SM, Kataria S, et al. Long-term outcomes of stereotactic body radiation therapy (SBRT) with fiducial tracking for inoperable stage I non-small cell lung cancer (NSCLC). *J Radiat Oncol*. 2016;5:379-387.

33. Koshy M, Malik R, Weichselbaum RR, Sher DJ. Increasing radiation therapy dose is associated with improved survival in patients undergoing stereotactic body radiation therapy for stage I non-small-cell lung cancer. *Int J Radiat Oncol Biol Phys*. 2015;91:344-350.

34. Stahl JM, Ross R, Harder EM, et al. The effect of biologically effective dose and radiation treatment schedule on overall survival in stage I non-small cell lung cancer patients treated with stereotactic body radiation therapy. *Int J Radiat Oncol Biol Phys*. 2016;96:1011-1020.

35. Onishi H, Araki T, Shirato H, et al. Stereotactic hypofractionated high-dose irradiation for stage I nonsmall cell lung carcinoma: Clinical outcomes in 245 subjects in a Japanese multiinstitutional study. *Cancer*. 2004;101:1623-1631.

36. Block AM, Luce J, Lin JY, Hoggarth MA, Roeske JC. Planar IGRT dose reduction: A practical approach. *Pract Radiat Oncol*. 2015;5:e239-e244.